Numerical simulation and parametric sensitivity study of titanium dioxide particles synthesised in a stagnation flame

Casper S. Lindberg[a,b], Manoel Y. Manuputty[a,b], Philipp Buerger[a], Jethro Akroyd[a,b], Markus Kraft[a,b,c,*]

[a] *Department of Chemical Engineering and Biotechnology, University of Cambridge, Philippa Fawcett Drive, Cambridge, CB3 0AS, United Kingdom*
[b] *CARES, Cambridge Centre for Advanced Research and Education in Singapore, 1 Create Way, CREATE Tower, #05-05, Singapore, 138602*
[c] *School of Chemical and Biomedical Engineering, Nanyang Technological University, 62 Nanyang Drive, Singapore, 637459*

Abstract

A detailed population balance model is used to simulate titanium dioxide nanoparticles synthesised in a stagnation flame from titanium tetraisopropoxide (TTIP) precursor. A two-step simulation methodology is employed to apply the detailed particle model as a post-process to flame profiles obtained from a fully coupled simulation with detailed gas-phase chemistry, flow dynamics and a simple particle model. The detailed particle model tracks the size and coordinates of each primary in an aggregate, and is able to resolve the particle morphology, permitting direct comparison with experimental measurements through simulated TEM-style images. New sintering parameters, informed by molecular dynamics simulations in the literature, are introduced into the model to account for the sintering behaviour of sub-10 nm particles. Simulated primary and aggregate particle size distributions were in excellent agreement with experimental measurements. A parametric sensitivity study found particle morphology to be sensitive to the sintering parameters, demonstrating the need to apply careful consideration to the sintering behaviour of nano-sized particles in modelling studies. The final particle morphology was not found to be sensitive to other model parameters.

*Corresponding author
Email address: mk306@cam.ac.uk (Markus Kraft)

Keywords: titanium dioxide, stagnation flame, population balance, sensitivity, sintering,

1. Introduction

The flame synthesis of metal oxide nanoparticles, such as titanium dioxide (titania, TiO_2), is an important process that has received significant focus in the research community and has many industrially relevant applications. Modelling studies, combined with experiments, provide a way to understand the complex processes involved in the formation and growth of nanoparticles, and to optimise and tailor their properties. Premixed stagnation flame experiments have been used to synthesise ultra-fine TiO_2 nanoparticles from titanium tetraisopropoxide (TTIP) with particle sizes of 4–15 nm (Tolmachoff et al., 2009; Memarzadeh et al., 2011; Manuputty et al., 2019a,b). The small particle size is a result of a short particle residence time and is therefore suitable for studying the early stages of particle formation. In addition, the pseudo one-dimensional flow makes it easier to couple the particle model with the gas-phase chemistry and flow dynamics.

Most attempts at modelling high temperature TiO_2 formation from TTIP assume a one-step thermal decomposition of TTIP. A first-order reaction rate was proposed by Okuyama et al. (1990) based on hot wall reactor studies at 400–600°C and has been supported by more recent studies (Wang et al., 2015; Korobeinichev et al., 2012). Tsantilis et al. (2002) later combined this with a surface decomposition reaction to model TiO_2 formation in a premixed flat flame. A similar reaction model has also been used in other studies (Yu et al., 2008; Zhao et al., 2009; Manuputty et al., 2017) with varying degrees of success. Experimental studies have shown that TTIP decomposition at flame temperature is a complex reaction involving many intermediate species (Shmakov et al., 2013). Thus, an accurate model of TiO_2 formation in a wide range of operating conditions relies on an accurate description of the gas-phase chemistry. A recent paper proposed a systematically derived and thermodynamically consistent detailed kinetic mechanism of TTIP decomposition (Buerger et al., 2017).

Previous simulations of the stagnation flame experiment (Manuputty et al., 2017) employed a spherical particle model and used the method of moments with interpolative closure (MoMIC) to solve the population balance equations. The approach permitted full coupling of the particles to the

gas-phase and flow dynamics. Such fully-coupled approaches are generally constrained to one or two internal coordinates in the particle description. Yet, particles are usually observed to be aggregate structures composed of a polydisperse population of primary particles with different levels of sintering. A multivariate model is needed to fully capture the particle morphology. However, multivariate particle models typically require stochastic numerical methods and do not easily incorporate particle transport and spatial inhomogeneity. One approach, used successfully to simulate soot formation in laminar flames (Singh et al., 2005; Morgan et al., 2007; Yapp et al., 2016; Chen et al., 2013) and recently extended to stagnation flames (Lindberg et al., 2019a; Hou et al., 2019), is a two-step post-processing methodology. First, the flame profile is solved in a fully coupled simulation with detailed chemistry, flow dynamics and a simple population balance model. Second, the flame profile is post-processed with a detailed particle model to resolve the particle morphology.

A detailed particle model allows for the simulation of quantities that are directly comparable to experimental data, such as particle size measurements from TEM imaging and mobility size analysis (Tsantilis et al., 2002; Arabi-Katbi et al., 2001; Zhao et al., 2007). For example, simulated TEM-style images can be analysed in a similar manner to experimental data to obtain the aggregate size distribution – as is done in this work. In addition, a detailed particle description permits the modelling and study of processes that are fundamental to the evolution of particle morphology, but which cannot be fully captured by simpler models. For instance, sintering is commonly modelled by considering the evolution of the surface area of an aggregate with a defined characteristic time (Koch and Friedlander, 1990); however, these models often extrapolate late stage behaviour over the entire process. More detailed geometrical models permit a more complete picture of the evolution of particles during sintering (Eggersdorfer et al., 2011, 2012; Yadha and Helble, 2004). Furthermore, the sintering behaviour is strongly influenced by the morphological properties of the particle, particularly at the nano-scale ($d_\mathrm{p} < 10$ nm). For example, in a molecular dynamics study on the sintering of 2–4 nm TiO_2, Buesser et al. (2011) found the sintering rate to be much faster than that predicted by extrapolating the characteristic sintering time typically used in studies on larger particles (Kobata et al., 1991; Seto et al., 1995). The stagnation flame setup, used to synthesise ultra-fine TiO_2 particles, provides an excellent system to study the behaviour of sintering models for very small particles.

The purpose of this paper is to evaluate a new detailed particle model for titanium dioxide nano-aggregates (Lindberg et al., 2019b) against experimental measurements (Manuputty et al., 2019b), and perform a parametric sensitivity study to understand the influence of key parameters on the particle properties. We simulate the synthesis of titanium dioxide nano-aggregates from TTIP precursor in a stagnation flame using a two-step simulation methodology (Lindberg et al., 2019a). A detailed chemical mechanism is used to describe the thermal decomposition of TTIP (Buerger et al., 2017) and a detailed particle model (Lindberg et al., 2019b) is used to resolve the particle morphology. The detailed particle description permits comparison of simulated quantities with equivalent experimental measurements; namely, the aggregate projected spherical equivalent diameter distribution (particle size distribution, PSD) and the primary particle size distribution (PPSD), obtained by TEM image analysis.

2. Experiment

A laminar stagnation flame, stabilised by flow stretch, was used to prepare TiO_2 nanoparticles from titanium tetraisopropoxide (TTIP) precursor. Full details of the experimental investigation are presented in (Manuputty et al., 2019b). The premixed gas was heated to 150°C with exit velocity of 436 cm/s. Premixed gas mixtures with two different equivalence ratios (ϕ) were used: $\phi = 0.35$, i.e. lean flames (3.5% C_2H_4–30% O_2–66.5% Ar) and $\phi = 1.67$, i.e. rich flames (10.3% C_2H_4–18.5% O_2–71.2% Ar). The TTIP loading rates used were 4, 12 and 30 ml/h, corresponding to 194, 582, and 1454 ppm TTIP respectively. These loading rates correspond to effective equivalence ratio (if TTIP is included in the equivalence ratio calculation) of 0.36, 0.39, and 0.44 for lean flames and 1.69, 1.73, and 1.81 for rich flames.

Particles were sampled through an orifice in the stagnation plate and diluted with nitrogen gas in the sample line to reduce aggregation. Nanoparticle morphology was characterised by analysing TEM images and mobility measurements. Details on the sampling procedure, dilution test and particle characterisation are reported in (Manuputty et al., 2019b), so are not repeated here. Overall, it was found that the particle morphology was sensitive to the TTIP loading but was relatively insensitive to the equivalence ratio. Here we choose five descriptors of particle morphology from the TEM image analysis for comparison with the simulation results. These are the mean ($\bar{d}_\mathrm{p}$) and coefficient of variation (CV_p) of the primary particle diame-

ter; mean ($\bar{d}_{\mathrm{a}}$) and coefficient of variation (CV_{a}) of the aggregate projected spherical equivalent diameter; and the fraction of aggregates with circular projection (f_α). The mean diameter, standard deviation and coefficient of variation are defined for N aggregate or primary particles as:

$$\bar{d} = \frac{1}{N}\sum_{i=1}^{N} d_i, \tag{1}$$

$$\mathrm{SD} = \sqrt{\frac{1}{N-1}\sum_{i=1}^{N}\left(d_i - \bar{d}\right)^2}, \tag{2}$$

$$\mathrm{CV} = \frac{\mathrm{SD}}{\bar{d}}. \tag{3}$$

The dimensionless coefficient of variation, or the ratio of the standard deviation to the mean, is used as a measure of the distribution widths in this work to allow for comparison across all TTIP loading rates, i.e. cases with varying mean sizes. The aggregate projected spherical equivalent diameter is

$$d_{\mathrm{a},i} = 2\sqrt{\frac{A_{\mathrm{a},i}}{\pi}}, \tag{4}$$

where $A_{\mathrm{a},i}$ is the aggregate projected area. As per Manuputty et al. (2019b), the parameter α_i is defined for an aggregate as the ratio of projected diameter of gyration, $d_{\mathrm{g},i}$, and the projected spherical equivalent diameter:

$$\alpha_i = \frac{d_{\mathrm{g},i}}{d_{\mathrm{a},i}}. \tag{5}$$

The fraction of aggregates with circular projection, f_α, is defined as the fraction of particles with $\alpha_i < 0.73$.

The uncertainties of the primary particle and aggregate sizes are based on the resolution limits of the images analysed, estimated as ± 4 and ± 2 pixels, respectively. These correspond to ± 0.48 nm for the primary sizes (all loadings) and ± 0.5 nm (4 ml/h TTIP), ± 0.64 nm (12 ml/h), and ± 0.94 nm (30 ml/h) for aggregate sizes. Lastly, temperature measurements were performed for this work in order to estimate the flame standing distance used in the simulation. The details of these measurements are given in the Supplementary Material.

3. Model

3.1. Flow model

The axisymmetric stagnation flow is modelled using a pseudo one-dimensional approximation as described in detail by Manuputty et al. (2017).

3.2. Chemical reaction model

The chemical reaction model consists of a TTIP decomposition mechanism combined with hydrocarbon combustion chemistry described by the USC-Mech II model (Wang et al., 2007). The TTIP mechanism contains 25 Ti species and 61 reactions, and describes the decomposition of TTIP to titanium (IV) hydroxide ($Ti(OH)_4$) through the C_3H_6 and CH_3 abstraction pathways identified by Buerger et al. (2017) as well as dissociation reactions of $Ti(OH)_4$, assumed to be barrierless. The estimated transport data and thermodynamic data of species (Buerger et al., 2017) are included in the Supplementary Material. In this work, $Ti(OH)_4$ is treated as the collision species for the particle inception and surface growth reactions in the particle model.

3.3. Population balance model

The two-step simulation methodology employed in this work uses two particle models. A simple one-dimensional model which characterises a particle by the number of constituent TiO_2 monomers is used in the first simulation step, and a detailed particle model is applied in a second step post-process. The detailed particle model is described in Section 3.3.1 below, and the two-step simulation methodology is outlined in Section 4. The dynamics of the particle population are described by the Smoluchowski coagulation equation with additional terms for inception, growth and sintering (Kraft, 2005). In both models, inception and surface growth are treated as collision limited processes with $Ti(OH)_4$ as the collision species. Sintering is only considered in the detailed model.

3.3.1. Detailed particle model

A comprehensive description of the detailed particle model is presented in (Lindberg et al., 2019b), so only a brief summary is given here. The type space of the detailed particle model is illustrated in Fig. 1. The type space is the mathematical description of a particle. An aggregate particle is composed of polydisperse primary particles modelled as overlapping spheres.

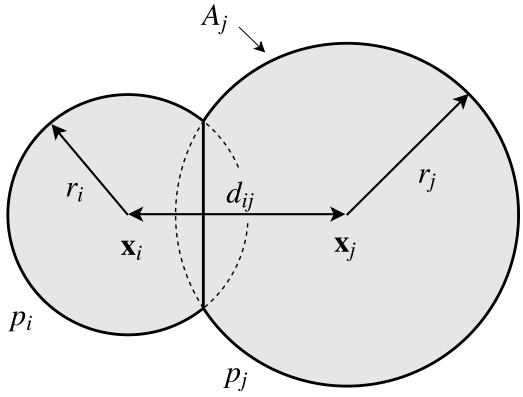

Figure 1: An illustration of the detailed particle model type space.

Each primary particle, p_i, is characterised by its composition η_i, radius r_i, and position of the primary centre $\mathbf{x}_i$. The degree of overlap between two neighbouring primaries, p_i and p_j, is then resolved by their centre to centre separation, $d_{ij} = |\mathbf{x}_i - \mathbf{x}_j|$.

Inception is modelled as a bimolecular collision of two $Ti(OH)_4$ molecules forming a particle containing two units of TiO_2. The rate of inception is given by the free molecular collision kernel with the $Ti(OH)_4$ collision diameter, $d_c = 0.5128$ nm, taken from the optimised geometry calculated in (Buerger et al., 2015).

An aggregate is formed when two particles stick together as a result of a collision. The rate of collision is calculated using the transition regime coagulation kernel (Patterson et al., 2006b). The orientations of the colliding particles and point of contact following the collision are determined by ballistic cluster-cluster aggregation with a random impact parameter (Jullien, 1984).

A particle may grow by consuming $Ti(OH)_4$ from the gas-phase and adding TiO_2 to the surface of a particle. The rate of growth is based on the free molecular collision kernel and assumes that the condensing species is much smaller than the particle. The mass of the species is assumed to be similar to that of TiO_2 and is added to a constituent primary particle p_j, selected with probability proportional to its free surface area A_j, relative to that of the entire aggregate.

Neighbouring primaries undergo sintering in which the primary centres approach each other, increasing their overlap. The mass of each individual

primary is conserved by increasing the primary radii. The sintering model follows the approach of Eggersdorfer et al. (2012) with the rate evaluated using a grain boundary diffusion model. Once sufficiently sintered, two primaries are assumed to coalesce to form a single primary. The threshold for coalescence is chosen to be

$$\frac{R_{ij}}{r_i} > 0.95, \tag{6}$$

where R_{ij} is the neck radius and $r_i \leq r_j$. It should be noted that the particle model does not distinguish between liquid and solid states. Consequently, the sintering process is applied even above the melting temperature of particles – conditions under which two particles would be expected to coalesce immediately upon collision. This liquid-like behaviour is achieved through rapid sintering kinetics arising from the temperature and size dependence of the modelled sintering rate, which is discussed in the next section.

3.3.2. Characteristic sintering time

Sintering is commonly modelled by considering the excess surface area of an aggregate over that of a sphere with the same mass (Xiong and Pratsinis, 1993; Kruis et al., 1993; Seto et al., 1995; Nakaso et al., 2001; West et al., 2009). The model of Koch and Friedlander (1990), valid for $t \gg \tau$, describes the evolution of the surface area:

$$\frac{\mathrm{d}A}{\mathrm{d}t} = -\frac{1}{\tau}(A - A_{\mathrm{sph}}), \tag{7}$$

where A is the surface area of the aggregate, A_{sph} is the surface area of a sphere with the same mass and τ is the characteristic sintering time. Multivariate particle models (Sander et al., 2009; Shekar et al., 2012) have extended this approach to consider the surface area of each pair of neighbouring primary particles individually. It should be noted that Eq. (7) applies to late stage sintering behaviour, but is often extrapolated to all stages of sintering.

If the characteristic sintering time τ is constant, Eq. (7) yields an exponential decay with τ corresponding to a 63% reduction in the excess surface area. However, in general τ does not remain constant, but varies as a function of temperature and particle diameter (Seto et al., 1995). Buesser et al. (2011) remark that the characteristic time is the time needed for the neck diameter to reach 83% of the initial primary particle diameter (Kobata et al., 1991), corresponding to a 67% reduction in the excess surface area and close to the commonly used exponential decay.

Various expressions for the characteristic sintering time of titanium dioxide particles have been proposed. Kobata et al. (1991) proposed a characteristic time based on a surface diffusion model:

$$\tau = 7.44 \times 10^{16} d_\mathrm{p}^4 T \exp\left(\frac{258\ \mathrm{kJ\,mol^{-1}}}{RT}\right)\ \mathrm{s}, \tag{8}$$

where d_p is the primary diameter (m), R the ideal gas constant and T is the temperature (K). Seto et al. (1995) considered a grain boundary diffusion based model with

$$\tau = 9.75 \times 10^{15} d_\mathrm{p}^4 T \exp\left(\frac{258\ \mathrm{kJ\,mol^{-1}}}{RT}\right)\ \mathrm{s}. \tag{9}$$

Both studies investigated particles larger than 10 nm, with Seto et al. (1995) noting that the sintering behaviour of nano-sized particles may be quite different.

Buesser et al. (2011) performed molecular dynamics simulations to study the sintering of 2–4 nm rutile particles at 1500–2000 K, and found that smaller nanoparticles ($d_\mathrm{p} < 4$ nm) sinter significantly faster than predicted by a d_p^4 dependence. They fitted a characteristic sintering time,

$$\tau = 3.7 \times 10^{16} d_\mathrm{p}^4 T \exp\left(\frac{258\ \mathrm{kJ\,mol^{-1}}}{RT}\left(1 - \left(\frac{3.4\ \mathrm{nm}}{d_\mathrm{p}} - \frac{T}{4100\ \mathrm{K}}\right)^{3.76}\right)\right)\ \mathrm{s}, \tag{10}$$

which includes a particle size dependence in the exponential term. This is consistent with an earlier theoretical study by Tsantilis et al. (2001) on the viscous flow sintering of silica particles, in which a particle size dependence was introduced to the activation energy based on the size dependence of the melting point:

$$\tau \propto \exp\left(\frac{E_\mathrm{a}}{RT}\left(1 - \frac{d_\mathrm{p,crit}}{d_\mathrm{p}}\right)\right). \tag{11}$$

The result is effectively instantaneous sintering below a critical diameter $d_\mathrm{p,crit}$. This form of the characteristic time has been used in multivariate particle models for silica (Sander et al., 2009; Shekar et al., 2012) and has also been applied to soot modelling (Chen et al., 2013; Yapp et al., 2015).

The preceding models considered the evolution of the surface area of an aggregate. In contrast, the detailed geometrical description used in this work (Lindberg et al., 2019b) requires the sintering equations to be formulated in

terms of the primary separations and radii. Following Eggersdorfer et al. (2012), the rate of change in primary centre to neck distance is

$$\frac{\mathrm{d}x_{ij}}{\mathrm{d}t} = -\frac{d_\mathrm{p}^4}{16\theta A_{\mathrm{n},ij}}\left(\frac{1}{r_i - x_{ij}} - \frac{1}{R_{ij}}\right), \tag{12}$$

where x_{ij} is the distance from the centre of primary p_i to the neck formed with neighbour p_j, $A_{\mathrm{n},ij}$ is the neck area, R_{ij} is the neck radius and r_i is the radius of the primary p_i. The characteristic time is

$$\theta = 9.11 \times 10^{17} d_\mathrm{p}^4 T A_\mathrm{s} \exp\left(\frac{258\ \mathrm{kJ\,mol^{-1}}}{RT}\left(1 - \left(\frac{d_{\mathrm{p,crit}}}{d_\mathrm{p}}\right)^{\alpha_\mathrm{crit}}\right)\right)\ \mathrm{s}. \tag{13}$$

where we previously introduced a critical diameter $d_{\mathrm{p,crit}}$ (Lindberg et al., 2019b), with a similar form to that proposed by Tsantilis et al. (2001). In this work, we introduce an additional prefactor A_s and critical exponent α_crit. The effect of these parameters is discussed in Section 5.3.1. The primary diameter d_p is taken as the smaller of the two primary diameters, $d_\mathrm{p} = \min(d_\mathrm{p}(p_i), d_\mathrm{p}(p_j))$.

It is important to note that the characteristic time defined in Eq. (13) for the centre to neck separation model is not directly comparable to the characteristic times in Eqs. (8)–(10), which are defined with respect to the change in excess surface area. A method of comparison is discussed in Appendix A.

4. Numerical methods

The stagnation flame is simulated using a two-step methodology (Lindberg et al., 2019a). In the first step, the flame is modelled using a one-dimensional stagnation flow approximation, coupled to detailed gas-phase chemistry and a simple population balance model solved using method of moments with interpolative closure (MoMIC). This is solved as a boundary-value problem using the *k*inetics® software package (CMCL Innovations, 2016). A solution-adapted grid refinement is used in order to achieve convergence with 240–260 grid points. The first simulation step is described in (Manuputty et al., 2017).

The one-dimensional stagnation flow formulation invokes a constant eigenvalue assumption which is only valid for a specific set of conditions (Bouvet et al., 2014; Johnson et al., 2015). This results in the predicted flame front

being shifted compared to the experiments. This can be circumvented by imposing the boundary conditions – if these are known – near the flame instead of at the nozzle exit as done by Bergthorson and Dimotakis (2007). Alternatively, Bouvet et al. (2014) show that the 1D solution approximates the 2D solution when an appropriate radial velocity gradient (or jet spreading rate) at the nozzle exit is imposed to recover the same flame front position as in the 2D simulation. The same approach is used here in which the boundary conditions are specified according to the experimental conditions (Manuputty et al., 2019b) and appropriate axial velocity gradients are chosen to reproduce the experimental flame standing distance for each case. The boundary conditions including burner exit temperature (T_0), velocity (u_0), velocity gradient (a_0), and the plate temperature (T_b) are summarised in Table 1.

Table 1: Boundary conditions imposed at nozzle exit (1 cm) and stagnation surface.

Case	T_0 (K)	u_0 (cm/s)	a_0 (1/s)	T_b (K)
$\phi = 0.35$, undoped	423.15	436	-245	503
$\phi = 0.35$, 4 ml/h TTIP	423.15	436	-230	503
$\phi = 0.35$, 12 ml/h TTIP	423.15	436	-185	503
$\phi = 0.35$, 30 ml/h TTIP	423.15	436	-99	503
$\phi = 1.67$, undoped	423.15	436	-185	580
$\phi = 1.67$, 4 ml/h TTIP	423.15	436	-185	580
$\phi = 1.67$, 12 ml/h TTIP	423.15	436	-215	580
$\phi = 1.67$, 30 ml/h TTIP	423.15	436	-280	580

In the second step, the resulting gas-phase profile is post-processed with the detailed particle model to resolve the aggregate morphology. The gas-phase profiles, supplied as input to the population balance simulation, are expressed in terms of the residence time of a Lagrangian particle travelling from the burner to stagnation plate using the combined convective and thermophoretic velocities. To account for the effect of thermophoretic transport near the stagnation surface, a thermophoretic correction is introduced to the post-process through a modified simulation sample volume scaling term. The thermophoretic correction is discussed in detail in (Lindberg et al., 2019a).

A stochastic numerical method is used in the second step to solve the population balance equations. The method employs a direct simulation algorithm (Shekar et al., 2012) with a majorant kernel and fictitious jumps

(Goodson and Kraft, 2002; Patterson et al., 2006b) to improve the computational speed of calculating the coagulation rate, and a linear process deferment algorithm (Patterson et al., 2006a) to provide an efficient treatment of sintering and surface growth. Simulation results are averaged over 4 runs, each with 8192 stochastic particles.

5. Results and discussion

5.1. Temperature profiles and flame location

The simulation of a stretch stabilised flame such as the one used in this study requires knowledge of the flame standing distance or temperature profiles due to the limitation of the one-dimensional stagnation flow approximation in capturing a non-parabolic flow profile (Bergthorson et al., 2005). However, in this study only temperature measurements for the undoped lean flame ($\phi = 0.35$) were available due to the thermocouple service temperature limit. In this work, the temperature measurements were used to estimate the point at which the temperature rises sharply for the lean ($\phi = 0.35$) flame and to adjust the boundary conditions in the simulation (with the energy equation solved) to reproduce this. The comparison between the simulated temperature profile for this flame and the flame image shows that the simulated H peak coincides with the point at which the flame intensity is half of the maximum intensity (see supplementary material). An arbitrary assumption is then made to use the same criteria to define the flame standing distance and to adjust the boundary conditions (Table 1) for all other cases because no temperature measurements for these cases are available.

Figure 2 shows the measured and simulated temperature profiles for the undoped lean flame ($\phi = 0.35$) showing good agreement in the combustion zone widths. A significant difference is observed in the profile shape and the maximum temperature. The measured temperature profile suggests that the calculated adiabatic flame temperature is reached earlier near the upstream edge of the flame while the simulated profile shows the temperature increases to a maximum point nearer to the stagnation plate. It is likely that the proximity of the peak temperature region to the stagnation plate (cold boundary) in the simulation results in a lower maximum temperature compared to the measured maximum temperature which is close to the adiabatic temperature. The origin of the discrepancy in the temperature profiles is unclear but a possible reason is the deviation from the one-dimensional stagnation flow solution. Another possible source of error in the temperature measurements

is the catalytic reaction on the uncoated thermocouple surface. Catalytic heating is expected to affect the region near the flame front where there is more unreacted premixed gas (Shaddix, 1999). This will result in artificially higher temperature estimates at the flame front, which is the case in this work. This can also explain the measured temperature that is slightly higher than the calculated adiabatic flame temperature. This will be investigated in a future work.

Figure 2 also shows the H concentration profiles of the simulated flames, one with the calculated temperature profile (black line) and another with an imposed temperature profile from the experimental measurement (red line). The higher temperature in the imposed temperature simulation results in a significantly higher H concentration compared to the calculated temperature simulation (by a factor of 4). However, the location of the maximum H concentration remains unchanged. It is found that this location (denoted by the vertical dotted line in Fig. 2) coincides with the flame standing distance measured from the flame image analysis (see Supplementary Material). Thus, an assumption is made here to use the peak H concentration from the simulation to define the flame standing distance for the rich flame ($\phi = 1.67$) where temperature profile measurements were not available. Furthermore, it is assumed that the addition of TTIP does not affect the flame standing distance due to the relatively small amount of TTIP used. The flame distances of the simulated flames with varying TTIP loading used in this work are summarised in Table 2. This was adjusted to match the measured flame distance (3.22 mm for $\phi = 0.35$ and 3.92 mm for $\phi = 1.67$) within the uncertainty range of ± 0.2 mm.

Table 2: Flame distances of the simulated flames, in mm, taken as the distance of the peak H concentration from the stagnation surface.

	$\phi = 0.35$			$\phi = 1.67$		
	4 ml/h (194 ppm)	12 ml/h (582 ppm)	30 ml/h (1454 ppm)	4 ml/h (194 ppm)	12 ml/h (582 ppm)	30 ml/h (1454 ppm)
Calculated T	3.21	3.17	3.27	4.00	4.00	3.98
Imposed T	3.21	3.21	3.27	-	-	-

In order to understand the effect of the temperature profile uncertainties on the simulated particle properties, three parameters related to the experimental measurements are investigated in this work. These are the profile shape, flame standing distance, and surface temperature.

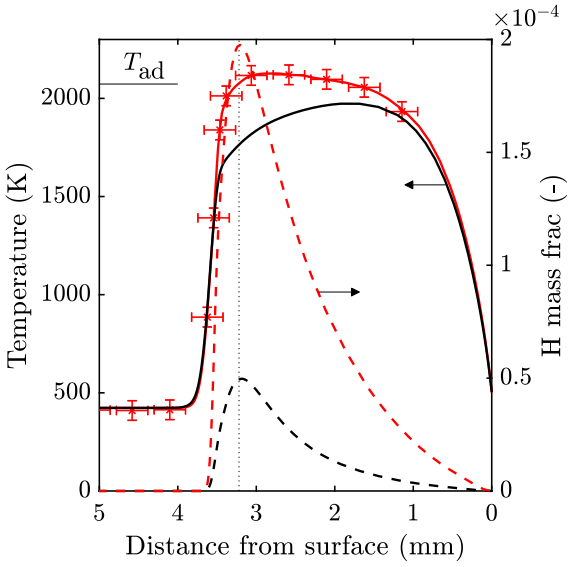

Figure 2: Temperature and H mass fraction profiles for $\phi = 0.35$ flame (no TTIP). The black lines are from the calculated temperature simulation and the red lines are from the imposed temperature simulation corresponding to the experimental measurements (symbols). The adiabatic flame temperature, T_{ad}, is annotated for comparison.

First, the effect of the temperature profile shape is assessed by comparing simulations with the calculated and the imposed temperature profiles. Figure 3 shows the temperature profiles for the lean flames with varying TTIP loading rate. For the 4 ml/h TTIP loading rate case, the imposed temperature profile is assumed to be the same as the measured profile for the undoped flame (symbols in Fig. 3). For the 12 and 30 ml/h cases, the temperature profiles are shifted upwards by 70 and 200 K, respectively, to account for the effect of TTIP combustion. These amounts of shift are approximately consistent with the shifts in the corresponding calculated temperature cases. Similar to the undoped flame case, the temperature profile shape does not seem to affect the flame standing distance (Table 2). The imposed temperature simulations are only attempted for the lean flames ($\phi = 0.35$) as no temperature measurement is available for the rich flame. In addition, the shape of the rich flame temperature profile is similar to the experimental profile in which the peak temperature is reached near the upstream edge of the flame (see for example Figs. S3 and S4).

Second, the effect of the flame distance is assessed by comparing simula-

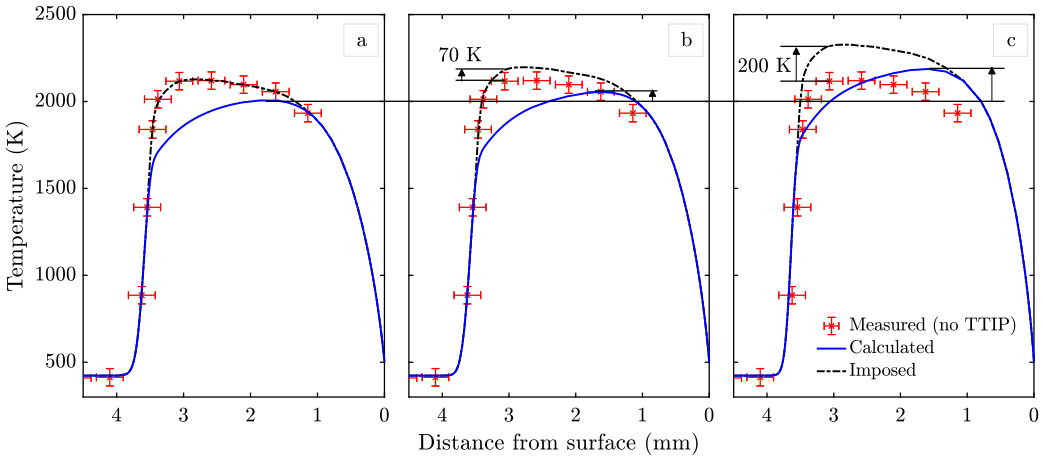

Figure 3: Calculated and imposed temperature profiles for $\phi = 0.35$ flames (a: 4 ml/h, b: 12 ml/h, c: 30 ml/h TTIP loading). The imposed temperature profile for 4 ml/h case is taken from experimental measurement (with no TTIP) while those for 12 ml/h and 30 ml/h cases are shifted by 70 and 200 K, respectively, similar to the shifts in the calculated maximum temperature profiles (arrows) to account for the additional heat release from TTIP combustion.

tions with varying flame distance (i.e. peak H concentration) by ± 0.2 mm with reference values in Table 2. This is approximately the same as the experimentally observed fluctuation in the flame front. The temperature profiles of these cases are shown in the Supplementary Material (Fig. S4). Finally, the effect of the surface temperature is assessed by comparing simulations with varying stagnation temperature by ± 50 K ($T_s = 503$ K for $\phi = 0.35$ and $T_s = 580$ K for $\phi = 1.67$ Manuputty et al. (2019b)). This uncertainty in the stagnation plate temperature comes from the fluctuation during experiment as well as a typical uncertainty for a K-type thermocouple.

Figure 4 presents the changes in primary particle and aggregate properties for all conditions tested in this work with respect to the uncertainties in the three temperature profile parameters discussed above. The model parameters used in the simulation will be discussed further in Section 5.3.1. Several observations are made here. First, all of the particle properties are insensitive to the shape of the temperature profile (imposed T vs. calculated T). Second, the mean primary and aggregate diameters are only sensitive to the flame distance – primarily the lean flame with high TTIP loading. Meanwhile, the coefficients of variation show very little sensitivity in all cases. f_α shows the greatest degree of sensitivity across the temperature profile pa-

rameters F_{d} and T_{s}. Overall, the changes in particle sizes are less than 1 nm, except for the lean flame with 30 ml/h TTIP loading (less than 2 nm). The maximum changes for CV and f_α are 1% and 3%, respectively. This suggests that the particle properties are relatively insensitive to the temperature profile parameters. More importantly, the changes in Fig. 4 give an indication of the degree of model prediction uncertainties carried forward from the uncertainties in experimental measurements feeding into the simulation, i.e. temperature and flame distance. These are referred to in this study as the "simulation uncertainties".

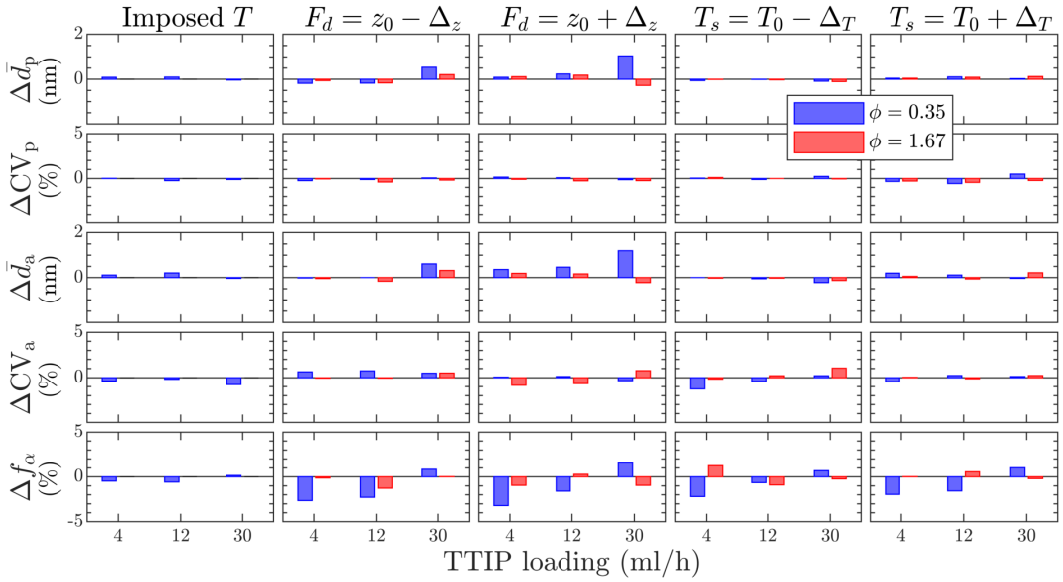

Figure 4: The changes in particle descriptors as the temperature profile shape (refer to text), flame distance, F_d, and surface temperature, T_s, are varied against the base case (calculated temperature, flame distance z_0, and surface temperature T_0) for all cases studied here. The particle descriptors are: (1) primary mean diameter, $\Delta\bar{d}_{\mathrm{p}}$, (2) primary coefficient of variation, $\Delta\mathrm{CV}_p$, (3) aggregate mean diameter $\Delta\bar{d}_{\mathrm{a}}$, (4) aggregate coefficient of variation, $\Delta\mathrm{CV}_{\mathrm{a}}$, and (5) fraction of particles with circular projection, Δf_α. The perturbations Δ_z and Δ_T are 0.2 mm and 50 K, respectively.

5.2. Particle temperature-time history

Figure 5 shows the evolution the mean primary diameter and mean aggregate collision diameter as a function of particle residence time for the six flames, using the base case model parameters given in Table 3. The collision

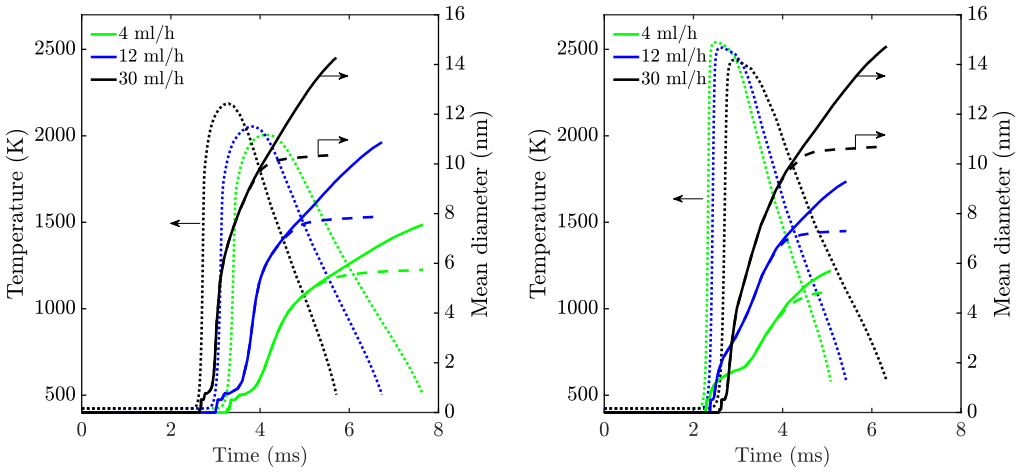

(a) Lean flame ($\phi = 0.35$). (b) Rich flame ($\phi = 1.67$).

Figure 5: Time evolution of mean primary diameter (dashed lines) and collision diameter (solid lines) for different TTIP loadings for (a) the lean and (b) the rich flames. The simulated temperature profiles (dotted lines) are included for reference.

diameter is defined as per (Lindberg et al., 2019b). It should be noted that this is not equivalent to the aggregate diameter obtained from image analysis that is used for comparison with the experimental data.

All flames show rapid growth in particle size as the temperature peaks, followed by slower growth as the temperature begins to decrease. The particles are initially single primaries – illustrated by the coincident primary and aggregate collision diameters. The subsequent deviation of the collision and primary diameters indicates the onset of aggregate formation as the sintering rate slows sufficiently relative to the rate of coagulation. This happens once the temperature falls into the 1500–2000 K range, with lower temperatures correlating with smaller mean particle size. At high temperature, the rapid sintering kinetics in the model cause near instantaneous coalescence and liquid-like behaviour of colliding particles. The observed range of transition temperatures is consistent with the melting point depression of nanoparticles (Guisbiers et al., 2008). After this point, primary growth effectively ceases and aggregates grow by coagulation.

We observe that the total residence time decreases with increasing maximum flame temperature, and the trend with respect to TTIP loading reverses

between the lean and the rich flames. Meanwhile, the trends in particle size with respect to TTIP loading are consistent across both flames. The higher loading cases show faster growth in particle size and larger final particle diameters. Both 30 ml/h cases show very similar particle evolution. However, the evolution of particles in the 4 ml/h cases differ substantially between the lean and the rich flames. The lean flame shows a significantly longer period of aggregate growth and larger final particle size as a consequence of the longer residence time.

5.3. Parametric sensitivity

5.3.1. Base case sintering parameters

The sensitivity of the aggregate and primary particle size distributions to three sintering parameters is investigated: the critical diameter $d_{\mathrm{p,crit}}$, prefactor A_{s}, and critical exponent α_{crit} (see Eq. (13)). The effect of varying each of the parameters on the sintering time is shown in Fig. 6. The characteristic sintering times τ of Kobata et al. (1991), Seto et al. (1995) and Buesser et al. (2011) (Eqs. (8)–(10), respectively) are also plotted. As noted in Section 3.3.2, these three characteristic sintering times cannot be directly compared to Eq. (13) (the characteristic time θ defined for the model used in this study) because the model equations are different (compare Eqs. (7) and (12)). To facilitate comparison, we determine a time τ for the present model, which is consistent with the typical use of Eqs. (8)–(10) in modelling work. In this case, τ is defined as the time needed to reduce the excess surface area of two equal sized primaries by 63% and corresponds to $\tau = 0.14\theta$ (see Appendix A).

The characteristic time τ is plotted as a function of primary diameter for two different temperatures. The temperatures are the minimum and maximum temperatures used in the molecular dynamics study of Buesser et al. (2011). The base case sintering parameters for this work (referred to as "sintering model 1") are chosen to give the best fit to the characteristic time of Buesser et al. (2011) (Eq. (10)). These values are: $A_{\mathrm{s}} = 0.25$, $d_{\mathrm{p,crit}} = 2.5$ nm and $\alpha_{\mathrm{crit}} = 7$. The shaded regions indicate the range over which the parameter is varied in the sensitivity study in Section 5.3.2.

Varying the prefactor results in a vertical shift in the characteristic time as shown by the shaded regions in Fig. 6(a). The effect of changing the critical diameter, shown in Fig. 6(b), changes the location of the asymptote and only affects the sintering time of small particles. The critical exponent α_{crit} affects the sharpness of the transition from large particle sintering behaviour

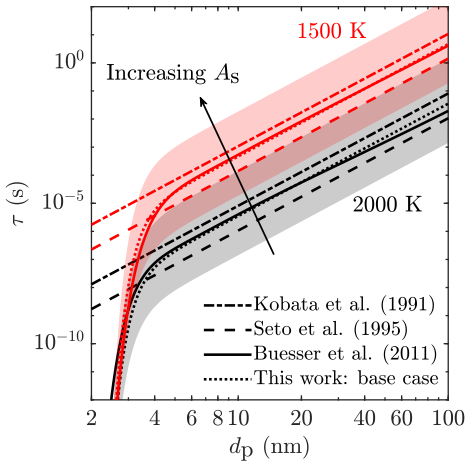

(a) Prefactor, $A_s = 0.01$–10.

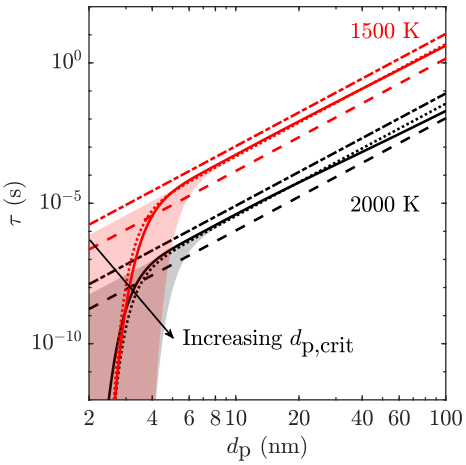

(b) Critical diameter, $d_{p,crit} = 0$–4 nm.

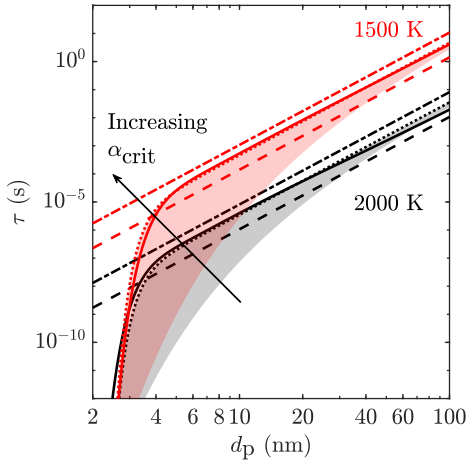

(c) Critical exponent, $\alpha_{crit} = 1$–7.

Figure 6: Effect of varying each sintering parameter on the characteristic sintering time. The base case parameters chosen for this study (dotted lines; $A_s = 0.25$, $d_{p,crit} = 2.5$ nm, $\alpha_{crit} = 7$) are a fit to the characteristic time of Buesser et al. (2011). The shaded regions indicate the range over which the parameter is varied. The characteristic times of Kobata et al. (1991) and Seto et al. (1995) are included for reference. $T = 1500$ K and $T = 2000$ K are the minimum and maximum of the range covered by the MD study in (Buesser et al., 2011).

($\tau \propto d_{\mathrm{p}}^4$) to near instantaneous sintering of small particles. A small exponent such as $\alpha_{\mathrm{crit}} = 1$, the lower bound of the shaded regions in Fig. 6(c), results in a long transition while larger values of α_{crit} create a sharper transition near the critical diameter. The consequence of a long transition is that the sintering time is reduced for particles significantly larger than the prescribed critical diameter; thus, near instantaneous sintering occurs for particles larger than the value of $d_{\mathrm{p,crit}}$ suggests. For example, Fig. 6(c) shows that the sintering time begins to deviate from a linear relationship for values of d_{p} that are an order of magnitude greater than $d_{\mathrm{p,crit}}$.

Simulated and experimental primary and aggregate particle size distributions are shown in Fig. 7 for the six flame conditions. The experimental particle size data, obtained by TEM image analysis, are from Manuputty et al. (2019b, Fig. 11). In the experimental investigation, primary particle diameters were measured by manually specifying the centre of a sphere and a point on the circumference. This measure is directly comparable to $d_{\mathrm{p},i} = 2r_i$ defined in the particle model (see Fig. 1). The aggregate size was obtained by measuring the two-dimensional projected area of each aggregate in the image to determine a projected spherical equivalent diameter. In order to directly compare our simulation results to this data, similar analysis was performed on simulated TEM-style images generated from the simulation data using the procedure described in (Lindberg et al., 2019b). 100 images were generated for each simulation with an average of 43 particles per image.

PSDs simulated using sintering model 1 are shown by the blue lines in Fig. 7. For comparison, the red lines show PSDs simulated with the sintering parameters used in an earlier work (Lindberg et al., 2019b): $A_{\mathrm{s}} = 1$, $d_{\mathrm{p,crit}} = 4$ nm and $\alpha_{\mathrm{crit}} = 1$ (henceforth referred to as "sintering model 2"). The other simulation parameters are summarised in Table 3. The simulated aggregate size distribution are similar for both sets of sintering parameters and are in good agreement with the experimental data. On the other hand, the primary particle size distributions are considerably different. Sintering model 1 yields very good agreement with the experimental data, while sintering model 2 produces a much wider PPSD at lower TTIP loading.

The effect on the width of the PPSD is also evident in the trend displayed by the coefficient of variation as a function of TTIP loading, plotted in Fig. 8. Sintering model 1 produces a trend that is consistent with the relatively flat trend shown by the experimental data. Model 2, however, displays a decreasing trend with a significantly larger CV at low TTIP loading. The trends observed in the mean primary and aggregate size, and aggregate CV

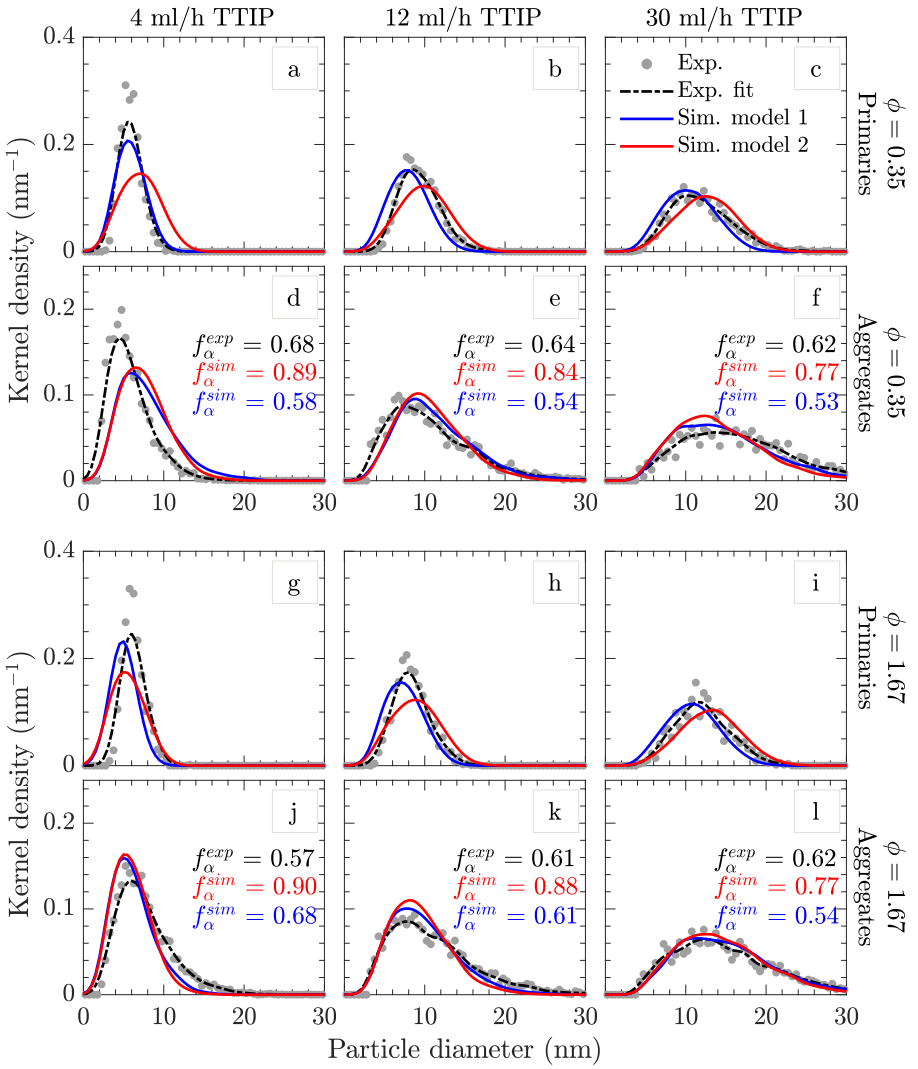

Figure 7: Simulated and measured primary and aggregate size distributions for the base case sintering parameters used in this work (sintering model 1, blue lines) and parameters from (Lindberg et al., 2019b) (sintering model 2, red lines). The experimental data points (Manuputty et al., 2019b, Fig. 11) are normalised particle counts with a bin width of 0.5 nm. The lines are from kernel distribution fits using 1 nm bandwidth. f_α denotes the fraction of spherical particles from TEM image analysis.

are consistent across both simulations and in reasonable agreement with the experimental data.

Another useful descriptor of particle morphology is the fraction of par-

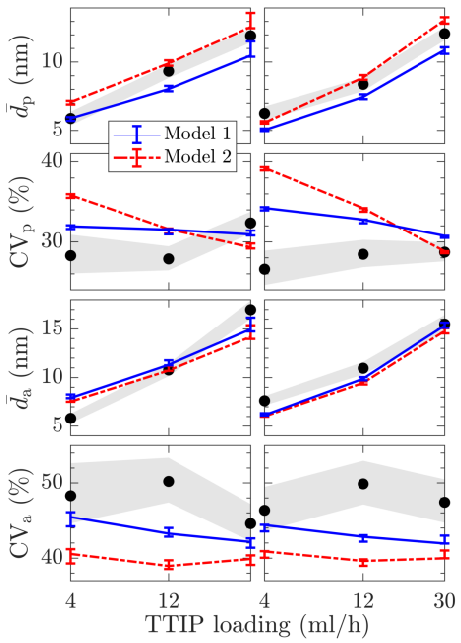

Figure 8: The primary and aggregate mean diameters and CVs for sintering model 1 (solid blue lines) and sintering model 2 (dashed red lines), for lean ($\phi = 0.35$, left panels) and rich ($\phi = 1.67$, right panels) flames. The shaded areas indicate estimated uncertainty bounds of the experimental measurements and error bars show the simulation uncertainties (see text).

ticles with circular projection f_α, defined in (Manuputty et al., 2019b), and shown in Fig. 7. The experimental results show a fairly constant fraction across both TTIP loading and equivalence ratio. In general, sintering model 1 slightly underpredicts the fraction of spherical particles (expect for the 4 ml/h rich flame case), while model 2 significantly overpredicts the fraction. Overall, simulations with sintering model 1 are in much better agreement with the experimental data. The largest discrepancy in f_α is seen in the 4 ml/h rich flame case. Sintering model 1 overpredicts the fraction of spherical particles by 11 percentage points, while model 2 overpredicts the fraction by 33 percentage points. The difference in predicted particle morphology is apparent in the TEM-style images presented in Fig. 9. Qualitatively, the TEM image produced with sintering model 1 (Fig. 9(b)) shows the presence of small aggregated particles, in agreement with the experimental TEM image for the same conditions (Manuputty et al., 2019b) (Fig. 9(a)), while the TEM image produced model 2 (Fig. 9(c)) shows mostly fully sintered spherical particles.

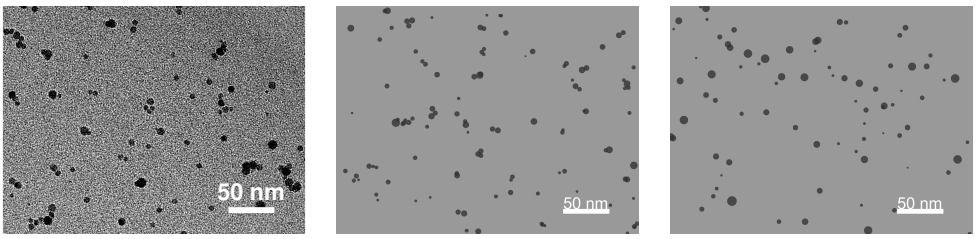

(a) Experimental TEM. (b) Sintering model 1. (c) Sintering model 2.

Figure 9: Experimental TEM and simulated TEM-style images for the rich flame ($\phi = 1.67$) with 4 ml/h TTIP loading.

This underscores the importance of comparing a range of morphological descriptors when evaluating simulation data against experiment. On the basis of the mean values alone, plotted in Fig. 8, sintering model 2 from (Lindberg et al., 2019b) may have been preferred; however, the CV and f_α suggest otherwise. The sensitivity to each individual sintering parameter and reasons for the observed trends in the descriptors will be investigated in the next section.

5.3.2. Sensitivity to sintering parameters

The sensitivity of the aggregate and primary mean diameter and CV to the sintering prefactor A_s are shown in Fig. 10. The base case values of the other parameters used in the simulation are given in Table 3. Overall, the descriptors are not particularly sensitive to the sintering prefactor, considering that it is varied over three orders of magnitude. Notably, the mean aggregate diameter shows almost no sensitivity to the sintering prefactor. This is unsurprising since sintering is an internal structural change and the aggregates are composed of a small number of primaries; thus, remain fairly compact in all configurations. The general insensitivity can to some extent be explained by the proximity of the average primary diameter to the critical diameter. In this region, the characteristic sintering time rapidly becomes less sensitive to the prefactor, as seen in Fig. 6(a).

Increasing the prefactor results in a narrower primary distribution with smaller mean size, but broader aggregate distribution. The effect is slightly more pronounced at higher TTIP loading due to the larger average particle size, which is farther from the critical diameter. Smaller A_s seems to give

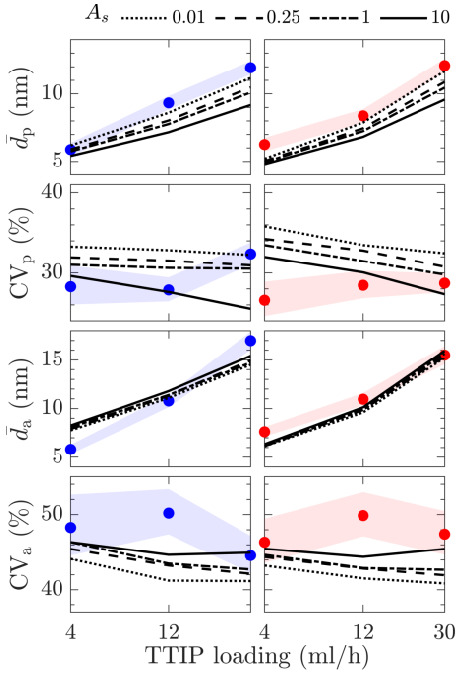

Figure 10: Sensitivity to the sintering prefactor A_s for lean ($\phi = 0.35$, left panels) and rich ($\phi = 1.67$, right panels) flames. The shaded areas indicate estimated uncertainty bounds of the experimental measurements.

better agreement with the experimental data in the mean primary size, but the width of the distribution is overestimated.

Figure 11 shows the sensitivity of the morphological descriptors to the critical sintering diameter. The mean primary and aggregate size, and aggregate CV are not particularly sensitive. In contrast, the primary coefficient of variation is sensitive to the choice of critical diameter, with larger values of $d_{p,crit}$ producing a smaller CV, indicating a narrower PPSD. This is because the critical diameter imposes an effective lower bound on the size of a primary in an aggregate (small primaries can of course exist as single particles). Lower TTIP loadings show greater sensitivity due to the average primary diameter being closer to the critical value. The results suggest that a value of $d_{p,crit} = 4$ nm is a better fit to the experimental data.

The effect of the critical exponent on the mean primary and aggregate diameter and coefficient of variation is shown in Fig. 12. The greatest sensitivity is observed between $\alpha_{crit} = 1$ and $\alpha_{crit} = 3$ for lower TTIP loading.

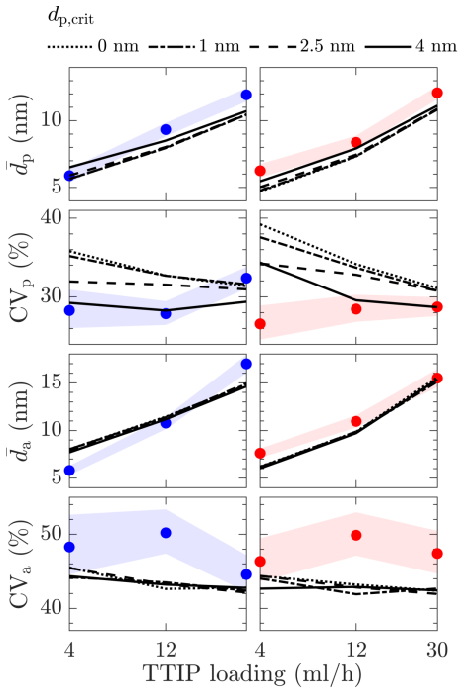

Figure 11: Sensitivity to the critical sintering diameter $d_{\mathrm{p,crit}}$ for lean ($\phi = 0.35$, left panels) and rich ($\phi = 1.67$, right panels) flames. The shaded areas indicate estimated uncertainty bounds of the experimental measurements.

This is notable in both CVs and the mean primary size. In particular, the decreasing trend in the primary CV as a function of TTIP loading changes to a relatively flat trend, which is more consistent with the experimental data. The reason for this is the fact that the mean primary size is close to the critical diameter; thus, the sharpness of the transition (see Fig. 6(c)) from large particle behaviour to instantaneous sintering has a significant impact on the evolution of the PPSD. For a large value of α_{crit}, instantaneous sintering only occurs at the tail of the distribution, thereby resulting in a narrower size distribution. With $\alpha_{\mathrm{crit}} = 1$, the sintering rate of large primaries is also increased significantly; thus, the entire size distribution evolves. The effect is most pronounced for the low TTIP loading cases due to their lower mean primary size, so more of the PPSD is located in this intermediate region around the transition.

The simulation results appear less sensitive to values larger than $\alpha_{\mathrm{crit}} = 3$; therefore, $\alpha_{\mathrm{crit}} = 3$ appears as reasonable a choice as $\alpha_{\mathrm{crit}} = 7$. In any case, a

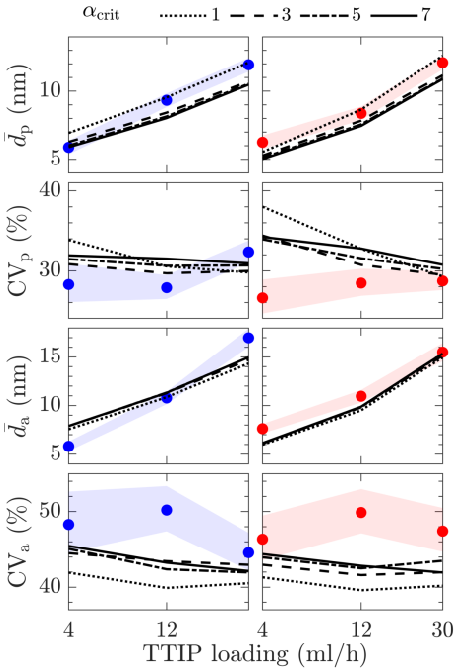

Figure 12: Sensitivity to the critical sintering exponent α_{crit} for lean ($\phi = 0.35$, left panels) and rich ($\phi = 1.67$, right panels) flames. The shaded areas indicate estimated uncertainty bounds of the experimental measurements.

reasonably sharp transition near the critical diameter is needed to obtain the correct sintering behaviour of particles near the transition. This is consistent with the fitted value of 3.76 obtained by Buesser et al. (2011). Their fitted sintering time also included an additional temperature dependence, which is not considered here.

5.3.3. Inception and surface growth efficiency

Sensitivity to the inception and growth efficiencies, γ_{in} and γ_{sg} respectively, was investigated over the range $\gamma = 0.01$–1. A bimodal primary size distribution, shown in Fig. 13, was observed in the lean flame simulations with small γ_{sg}. The minor mode of small primaries is more pronounced in simulations with smaller γ_{sg} and lower TTIP loading. The mode arises due to inception from unreacted $Ti(OH)_4$ near the stagnation surface, which is still present in the mixture due to very slow consumption by the growth process (see $Ti(OH)_4$ profiles in Fig. S5). No bimodality was seen in the rich flame simulations, possibly due to the higher reaction temperature increasing the

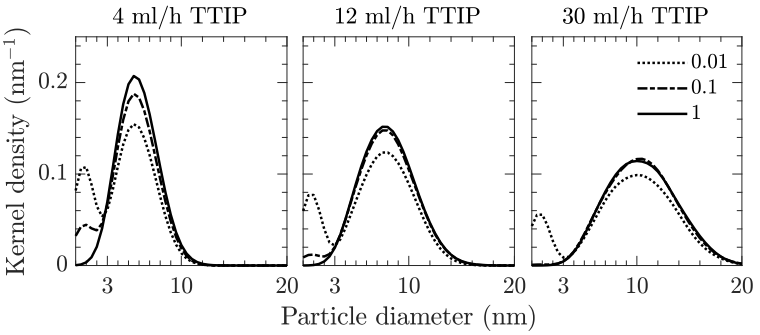

Figure 13: The bimodality of the primary particle distributions in lean flames ($\phi = 0.35$) with varying γ_{sg}.

consumption rates. This would also explain why the mode is less prominent at higher TTIP loading for $\gamma_{\mathrm{sg}} = 0.1$ (see simulated temperature profiles in the Supplementary Material). The bimodality is not present in the modelled aggregate size distributions due to the small particles falling below the size threshold for image analysis. Given the mode exists near the resolution limit of the experimental results, the presence of a small particle mode cannot be ruled out. This will be investigated in a future study.

Sensitivity to the inception and growth efficiencies are shown in Fig. 14 and Fig. 15, respectively. Note that the small particle mode in the $\gamma_{\mathrm{sg}} < 1$ cases is excluded from this analysis. The results show no sensitivity to either parameter. This is unsurprising if we consider how the particle processes compete with each other during the early stages of particle evolution. A particle is first formed by inception and can then grow either through the surface growth process or by coagulation with other particles. Sintering is effectively instantaneous in the high temperature region so the particle remains spherical following coagulation; therefore, the morphology of the particle is not influenced by the particular route taken (see flame profiles in Fig. 5). Inception and growth are competing for the same gas-phase species so adjusting the collision efficiency of one process primarily affects the relative rates. The overall rate remains sufficiently rapid (except for the lean flame with very small γ_{sg}) to consume the precursor before aggregate formation and sintering become significant; thus, the final morphology is unaffected.

These results appear to contradict observations in earlier modelling studies, which reported significant sensitivity to the rate of surface reaction (Tsantilis et al., 2002; Manuputty et al., 2017). However, the observations at the

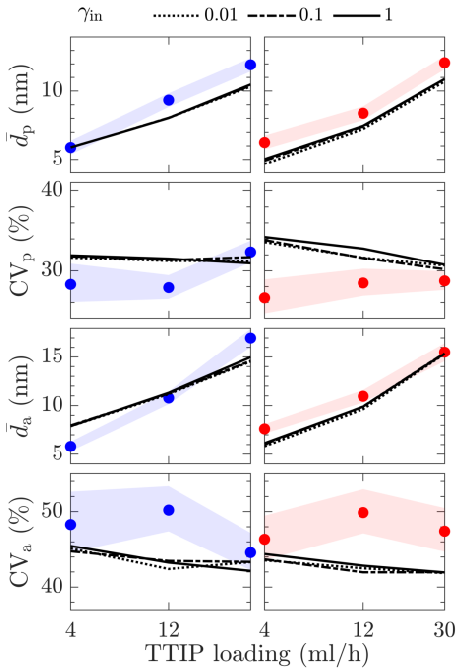

Figure 14: Sensitivity to the inception efficiency γ_{in} for lean ($\phi = 0.35$, left panels) and rich ($\phi = 1.67$, right panels) flames. The shaded areas indicate estimated uncertainty bounds of the experimental measurements.

stagnation surface do not give the full picture. Figure 16 shows the evolution of the mean primary diameter as a function of particle residence time. In the high temperature region, the mean primary diameter displays a high degree of sensitivity to both γ_{in} and γ_{sg}. As the temperature decreases near the stagnation surface, the different cases begin to converge towards the same final diameter, explaining the previously observed insensitivity. This is especially apparent in the rich flame ($\phi = 1.67$) simulations, but not as clear in the lean flame simulations due to the formation of the small particle mode, which causes a decrease in the mean diameter near the stagnation surface.

The behaviour seen here is consistent with the findings of Tsantilis et al. (2002), who, for a premixed flat flame, found that the sensitivity to the surface reaction could only be observed from measurements made near the burner. Further along the flame, the mean primary diameter was found to be much less sensitive to the surface reaction due to the dominance of coagulation.

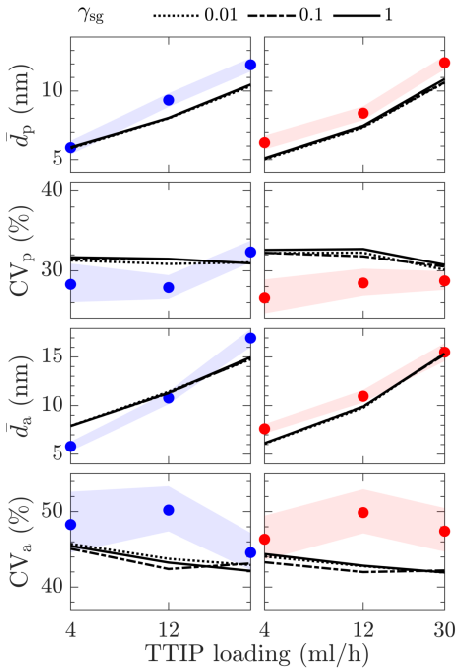

Figure 15: Sensitivity to the surface growth efficiency γ_{sg} for lean ($\phi = 0.35$, left panels) and rich ($\phi = 1.67$, right panels) flames. The shaded areas indicate estimated uncertainty bounds of the experimental measurements. A cutoff point of 2.5 nm is applied here for primary particle sizes to remove the first distribution mode observed for lean flames.

5.3.4. Summary

A summary of the parameters studied is provided in Table 3. The base case value, range over which the parameter was varied, and an indication of the observed sensitivity are given. Sensitivity analysis for the collision enhancement factor ϵ and density ρ is presented in the Supplementary Material. The base case value for the enhancement factor was taken as $\epsilon = 2.64$ (Zhang et al., 2011) and density is that of anatase $\rho = 3.84$ g/cm^3.

Overall, the particle morphology was found to be most sensitive to the choice of sintering parameters; in particular, the critical diameter and critical exponent due to the proximity of the average particle size to the critical size. Furthermore, the analysis suggested a larger value for the critical diameter $d_{p,crit} = 4$ nm, and a smaller value for the critical exponent $\alpha_{crit} = 3$ would be more appropriate. These are consistent with results from molecular dynamics studies (Buesser et al., 2011). The mean aggregate size was not affected by any of the three sintering parameters. This is unsurprising since the sintering

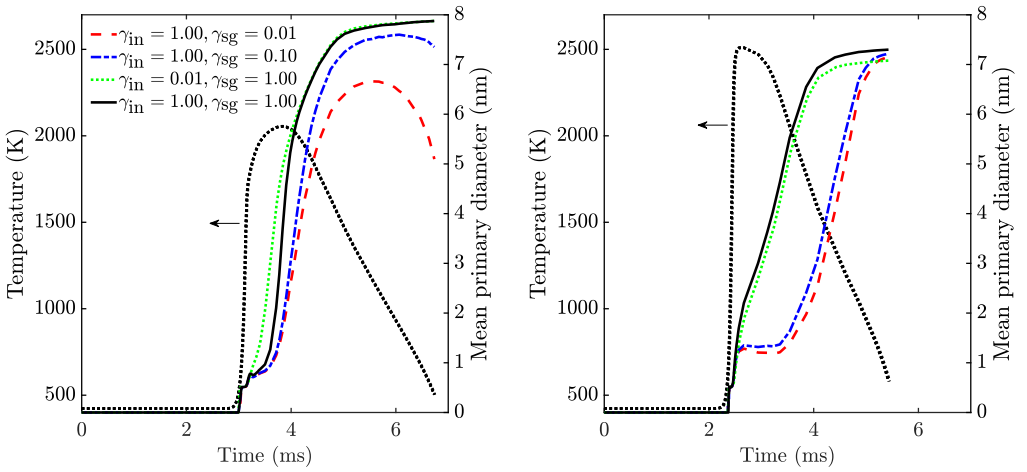

(a) Lean flame ($\phi = 0.35$), 12 ml/h TTIP loading.

(b) Rich flame ($\phi = 1.67$), 12 ml/h TTIP loading.

Figure 16: Evolution of mean primary size for different values of γ_{in} and γ_{sg} as a function of particle residence time. The temperature profile is included for reference.

process is an internal structural change.

The sensitivity analysis of the inception and surface growth parameters suggests that the final PSD at the stagnation surface is largely insensitive to the reaction mechanisms governing particle evolution early on in the flame. Experimental measurements from inside the combustion zone would be needed to discriminate between different models and parameters. A bimodal distribution at very small γ_{sg} was observed in the lean flame simulation; but, the small particle mode was too near the resolution limit of the experimental results to draw conclusions from the comparison.

Slight sensitivity was shown to the collision enhancement factor over the range studied, as expected, but not enough to discriminate between different values. It should be noted that the collision efficiency of titania nanoparticles has been shown to be strongly size and temperature dependent (Zhang et al., 2011; Sharma et al., 2018), and necessitates a more detailed investigation.

6. Conclusions

In this paper, we simulated the synthesis of titanium dioxide nano-aggregates from TTIP precursor in a premixed stagnation flame using a new detailed

Table 3: Summary of parametric sensitivity. The base case value, range studied and an indication of the sensitivity (++: sensitive; +: slightly sensitive; −: insensitive) are given. The sintering base case values correspond to sintering model 1.

Parameter	Value	Range	Sensitivity
Experimental parameters:			
Flame standing distance	Table 2	±0.2 mm	-
Surface temperature	503, 580 K	±50 K	-
Temperature profile shape	Calculated	Calculated/imposed	-
Sintering:			
Prefactor, A_s	0.25	0.01–10	+
Critical diameter, $d_{p,crit}$	2.5 nm	1–4 nm	++
Critical exponent, α_{crit}	7	1–7	++
Collision limited processes:			
Enhancement factor, ϵ	2.64	2.2–3.0	+
Inception efficiency, γ_{in}	1	0.01–1	-
Surface growth efficiency, γ_{sg}	1	0.01–1	-
Other:			
Density, ρ	3.84 g/cm^3	3.84, 4.25 g/cm^3	-

population balance model and two-step simulation methodology. A detailed chemical mechanism was used to describe the thermal decomposition of TTIP. Six flame cases from an earlier experimental investigation (Manuputty et al., 2019b) were simulated: a lean and a rich flame, each at three different precursor loadings. The detailed description of particle morphology in the population balance model was exploited to make direct comparisons with experimental measurements of primary and aggregate size distributions. Simulated TEM-style images were analysed in an identical manner to the original experimental procedure to obtain an aggregate size distribution based on the projected particle area; and the modelled primary particle size distribution was compared to the corresponding PPSD obtained from TEM image analysis in the experimental work. The simulated primary and aggregate particle size distributions were in excellent agreement with the experimental data.

The ultra-fine particles produced by the stagnation flame provided an excellent test case to investigate the characteristic sintering time of very small particles. New sintering parameters, informed by the molecular dy-

namics simulations of Buesser et al. (2011), were introduced into the model to account for the faster sintering behaviour of nano-sized particles. Three parameters were considered: a multiplicative prefactor; a critical diameter below which sintering becomes effectively instantaneous; and a critical exponent to control the transition from the large particle to small particle sintering behaviour. Simulation results with the new sintering parameters significantly improved the agreement with the experimental data, compared to parameters used in a previous work.

A parametric sensitivity study was performed to investigate the importance of individual model parameters. Particle morphology was found to be most sensitive to the critical sintering diameter and critical exponent, demonstrating the need to give careful consideration to the form of the characteristic time when the average particle size is at the transition from large particle sintering behaviour to the near instantaneous coalescence of nano-sized particles. Other model parameters, notably the inception and growth efficiencies, were found to not affect the final particle properties, despite the simulations showing significant sensitivity to these two parameters in the combustion zone. In a future work, it would be insightful to compare model prediction with experimental measurements from the combustion zone, and to investigate the effect of temperature and particle size on the collision efficiency.

Supplementary material

Additional details of the flame measurements, simulated flame profiles and parameteric sensitivity study are provided in the Supplementary Material. The TTIP decomposition mechanism used in this work is available via the University of Cambridge data repository at doi:10.17863/CAM.39744.

Acknowledgements

This project is supported by the National Research Foundation (NRF), Prime Minister's Office, Singapore under its Campus for Research Excellence and Technological Enterprise (CREATE) programme. The authors also thank Venator and CMCL Innovations for generous financial support. Markus Kraft acknowledges the support of the Alexander von Humboldt foundation.

Appendix A. Sintering model comparison

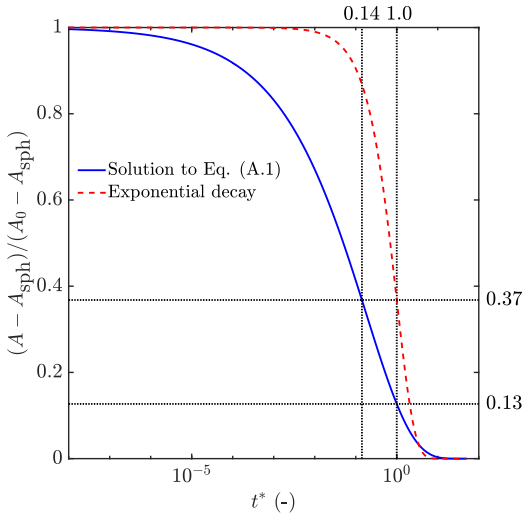

Figure A.17: The normalised excess surface area as a function of dimensionless time for the sintering of two equal sized primaries evolving according to Eq. (A.1). An exponential decay is plotted for reference.

The sintering model equation (Eq. (12)) is expressed in terms of the dimensionless time:

$$\frac{\mathrm{d}x_{ij}}{\mathrm{d}t^*} = -\frac{d_{\mathrm{p}}^4}{16A_{\mathrm{n},ij}}\left(\frac{1}{r_i - x_{ij}} - \frac{1}{R_{ij}}\right), \tag{A.1}$$

where

$$t^* = \frac{t}{\theta}. \tag{A.2}$$

The evolution of the normalised excess surface area of two equal sized particles sintering according to Eq. (A.1) is plotted in Fig. A.17 as a function of t^*. Equation (A.1) was solved using the Euler method. The solution was found to be insensitive to the choice of initial primary diameter. An exponential decay, the solution to Eq. (7) assuming a constant characteristic time, is plotted for reference. The two models show quite different behaviour, particularly at early times. The primary separation based model used in this work predicts a reduction in excess surface area of 87% over its characteristic time θ compared to the 63% reduction of an exponential decay.

To facilitate comparison of characteristic sintering times typically used in surface area based models (Koch and Friedlander, 1990) with the primary separation based model used in this work, a consistent definition of the characteristic sintering time is needed. In this case, we extract a value for τ from Fig. A.17 for the sintering model used here. τ is defined as the time needed for the excess surface area of two equal sized primaries to decrease by 63% – consistent with Eqs. (8)–(10) (Kobata et al., 1991; Seto et al., 1995; Buesser et al., 2011). For the primary separation based model used in this work,

$$\tau = 0.14\theta. \tag{A.3}$$

References

Arabi-Katbi, O.I., Pratsinis, S.E., Morrison, P.W., Megaridis, C.M., 2001. Monitoring the flame synthesis of TiO_2 particles by in-situ FTIR spectroscopy and thermophoretic sampling. Combust. Flame 124, 560–572. doi:doi:10.1016/S0010-2180(00)00227-3.

Bergthorson, J.M., Dimotakis, P.E., 2007. Premixed laminar C_1-C_2 stagnation flames: Experiments and simulations with detailed thermochemistry models. Proc. Combust. Inst. 31 I, 1139–1147. doi:doi:10.1016/j.proci.2006.07.110.

Bergthorson, J.M., Sone, K., Mattner, T.W., Dimotakis, P.E., Goodwin, D.G., Meiron, D.I., 2005. Impinging laminar jets at moderate Reynolds numbers and separation distances. Phys. Rev. E 72, 066307. doi:doi:10.1103/PhysRevE.72.066307.

Bouvet, N., Davidenko, D., Chauveau, C., Pillier, L., Yoon, Y., 2014. On the simulation of laminar strained flames in stagnation flows: 1D and 2D approaches versus experiments. Combust. Flame 161, 438–452. doi:doi:10.1016/j.combustflame.2013.09.010.

Buerger, P., Nurkowski, D., Akroyd, J., Kraft, M., 2017. A kinetic mechanism for the thermal decomposition of titanium tetraisopropoxide. Proc. Combust. Inst. 36, 1019–1027. doi:doi:10.1016/j.proci.2016.08.062.

Buerger, P., Nurkowski, D., Akroyd, J., Mosbach, S., Kraft, M., 2015. First-principles thermochemistry for the thermal decomposition of titanium tetraisopropoxide. J. Phys. Chem. A 119, 8376–8387. doi:doi:10.1021/acs.jpca.5b01721.

Buesser, B., Gröhn, A.J., Pratsinis, S.E., 2011. Sintering rate and mechanism of TiO_2 nanoparticles by molecular dynamics. J. Phys. Chem. C 115, 11030–11035. doi:doi:10.1021/jp2032302.

Chen, D., Zainuddin, Z., Yapp, E., Akroyd, J., Mosbach, S., Kraft, M., 2013. A fully coupled simulation of PAH and soot growth with a population balance model. Proc. Combust. Inst. 34, 1827–1835. doi:doi:10.1016/j.proci.2012.06.089.

CMCL Innovations, 2016. *k*inetics®. URL: `http://www.cmclinnovations.com/`.

Eggersdorfer, M.L., Kadau, D., Herrmann, H.J., Pratsinis, S.E., 2011. Multiparticle sintering dynamics: From fractal-like aggregates to compact structures. Langmuir 27, 6358–6367. doi:doi:10.1021/la200546g.

Eggersdorfer, M.L., Kadau, D., Herrmann, H.J., Pratsinis, S.E., 2012. Aggregate morphology evolution by sintering: Number and diameter of primary particles. J. Aerosol Sci. 46, 7–19. doi:doi:10.1016/j.jaerosci.2011.11.005.

Goodson, M., Kraft, M., 2002. An efficient stochastic algorithm for simulating nano-particle dynamics. J. Comput. Phys. 183, 210–232. doi:doi:10.1006/jcph.2002.7192.

Guisbiers, G., Van Overschelde, O., Wautelet, M., 2008. Theoretical investigation of size and shape effects on the melting temperature and energy bandgap of TiO2nanostructures. Appl. Phys. Lett. 92, 103121. doi:doi:10.1063/1.2897297.

Hou, D., Lindberg, C.S., Manuputty, M.Y., You, X., Kraft, M., 2019. Modelling soot formation in a benchmark ethylene stagnation flame with a new detailed population balance model. Combust. Flame 203, 56–71. doi:doi:10.1016/j.combustflame.2019.01.035.

Johnson, R.F., Vandine, A.C., Esposito, G.L., Chelliah, H.K., 2015. On the axisymmetric counterflow flame simulations: Is there an optimal nozzle diameter and separation distance to apply quasi one-dimensional theory? Combust. Sci. Technol. 187, 37–59. doi:doi:10.1080/00102202.2014.972503.

Jullien, R., 1984. Transparency effects in cluster-cluster aggregation with linear trajectories. J. Phys. A: Math. Gen. 17, L771–L776. doi:doi:10.1088/0305-4470/17/14/009.

Kobata, A., Kusakabe, K., Morooka, S., 1991. Growth and transformation of TiO_2 crystallites in aerosol reactor. AIChE J. 37, 347–359. doi:doi:10.1002/aic.690370305.

Koch, W., Friedlander, S.K., 1990. The effect of particle coalescence on the surface-area of a coagulating aerosol. J. Colloid Interface Sci. 140, 419–427. doi:doi:10.1016/0021-9797(90)90362-R.

Korobeinichev, O.P., Shmakov, A.G., Maksyutov, R.A., Tereshchenko, A.G., Knyazkov, D.A., Bolshova, T.A., Kosinova, M.L., Sulyaeva, V.S., Wu, J.S., 2012. Synthesis of mesoporous nanocrystalline TiO_2 films in a premixed $H_2/O_2/Ar$ flame. Combust. Explos. Shock Waves 48, 49–56. doi:doi:10.1134/S0010508212010078.

Kraft, M., 2005. Modelling of particulate processes. KONA Powder Part. J. 23, 18–35. doi:doi:10.14356/kona.2005007.

Kruis, F.E., Kusters, K.A., Pratsinis, S.E., Scarlett, B., 1993. A simple model for the evolution of the characteristics of aggregate particles undergoing coagulation and sintering. Aerosol Sci. Technol. 19, 514–526. doi:doi:10.1080/02786829308959656.

Lindberg, C.S., Manuputty, M.Y., Akroyd, J., Kraft, M., 2019a. A two-step simulation methodology for modelling stagnation flame synthesised aggregate nanoparticles. Combust. Flame 202, 143–153. doi:doi:10.1016/j.combustflame.2019.01.010.

Lindberg, C.S., Manuputty, M.Y., Yapp, E.K.Y., Akroyd, J., Xu, R., Kraft, M., 2019b. A detailed particle model for polydisperse aggregate particles. J. Comp. Phys. 397, 108799. doi:doi:10.1016/j.jcp.2019.06.074.

Manuputty, M.Y., Akroyd, J., Mosbach, S., Kraft, M., 2017. Modelling TiO_2 formation in a stagnation flame using method of moments with interpolative closure. Combust. Flame 178, 135–147. doi:doi:10.1016/j.combustflame.2017.01.005.

Manuputty, M.Y., Dreyer, J.A.H., Sheng, Y., Bringley, E.J., Botero, M.L., Akroyd, J., Kraft, M., 2019a. Polymorphism of nanocrystalline TiO_2 prepared in a stagnation flame: Formation of TiO_2-II phase. Chem. Sci. 10, 1342–1350. doi:doi:10.1039/C8SC02969E.

Manuputty, M.Y., Lindberg, C.S., Botero, M.L., Akroyd, J., Kraft, M., 2019b. Detailed characterisation of TiO_2 nano-aggregate morphology using TEM image analysis. J. Aerosol Sci. 133, 96–112. doi:doi:10.1016/j.jaerosci.2019.04.012.

Memarzadeh, S., Tolmachoff, E.D., Phares, D.J., Wang, H., 2011. Properties of nanocrystalline TiO_2 synthesized in premixed flames stabilized on a rotating surface. Proc. Combust. Inst. 33, 1917–1924. doi:doi:10.1016/j.proci.2010.05.065.

Morgan, N., Kraft, M., Balthasar, M., Wong, D., Frenklach, M., Mitchell, P., 2007. Numerical simulations of soot aggregation in premixed laminar flames. Proc. Combust. Inst. 31, 693–700. doi:doi:10.1016/j.proci.2006.08.021.

Nakaso, K., Fujimoto, T., Seto, T., Shimada, M., Okuyama, K., Lunden, M.M., 2001. Size distribution change of titania nano-particle agglomerates generated by gas phase reaction, agglomeration, and sintering. Aerosol Sci. Technol. 35, 929–947. doi:doi:10.1080/02786820126857.

Okuyama, K., Ushio, R., Kousaka, Y., Flagan, R.C., Seinfeld, J.H., 1990. Particle generation in a chemical vapor deposition process with seed particles. AIChE J. 36, 409–419. doi:doi:10.1002/aic.690360310.

Patterson, R.I.A., Singh, J., Balthasar, M., Kraft, M., Norris, J.R., 2006a. The linear process deferment algorithm: A new technique for solving population balance equations. SIAM J. Sci. Comput. 28, 303–320. doi:doi:10.1137/040618953.

Patterson, R.I.A., Singh, J., Balthasar, M., Kraft, M., Wagner, W., 2006b. Extending stochastic soot simulation to higher pressures. Combust. Flame 145, 638–642. doi:doi:10.1016/j.combustflame.2006.02.005.

Sander, M., West, R.H., Celnik, M.S., Kraft, M., 2009. A detailed model for the sintering of polydispersed nanoparticle agglomerates. Aerosol Sci. Technol. 43, 978–989. doi:doi:10.1080/02786820903092416.

Seto, T., Shimada, M., Okuyama, K., 1995. Evaluation of sintering of nanometer-sized titania using aerosol method. Aerosol Sci. Technol. 23, 183–200. doi:doi:10.1080/02786829508965303.

Shaddix, C.R., 1999. Correcting thermocouple measurements for radiation loss: a critical review. Proc. 33rd Natl. Heat Transf. Conf. .

Sharma, G., Dhawan, S., Reed, N., Chakrabarty, R., Biswas, P., 2018. Collisional growth rate and correction factor for TiO_2 nanoparticles at high temperatures in free molecular regime. J. Aerosol Sci. 127, 27–37. doi:doi:10.1016/j.jaerosci.2018.10.002.

Shekar, S., Menz, W.J., Smith, A.J., Kraft, M., Wagner, W., 2012. On a multivariate population balance model to describe the structure and composition of silica nanoparticles. Comput. Chem. Eng. 43, 130–147. doi:doi:10.1016/j.compchemeng.2012.04.010.

Shmakov, A.G., Korobeinichev, O.P., Knyazkov, D.A., Paletsky, A.A., Maksyutov, R.A., Gerasimov, I.E., Bolshova, T.A., Kiselev, V.G., Gritsan, N.P., 2013. Combustion chemistry of $Ti(OC_3H_7)_4$ in premixed flat burner-stabilized $H_2/O_2/Ar$ flame at 1 atm. Proc. Combust. Inst. 34, 1143–1149. doi:doi:10.1016/j.proci.2012.05.081.

Singh, J., Balthasar, M., Kraft, M., Wagner, W., 2005. Stochastic modeling of soot particle size and age distributions in laminar premixed flames. Proc. Combust. Inst. 30, 1457–1464. doi:doi:10.1016/j.proci.2004.08.120.

Tolmachoff, E.D., Abid, A.D., Phares, D.J., Campbell, C.S., Wang, H., 2009. Synthesis of nano-phase TiO_2 crystalline films over premixed stagnation flames. Proc. Combust. Inst. 32, 1839–1845. doi:doi:10.1016/j.proci.2008.06.052.

Tsantilis, S., Briesen, H., Pratsinis, S.E., 2001. Sintering time for silica particle growth. Aerosol Sci. Technol. 34, 237–246. doi:doi:10.1080/02786820150217812.

Tsantilis, S., Kammler, H.K., Pratsinis, S.E., 2002. Population balance modeling of flame synthesis of titania nanoparticles. Chem. Eng. Sci. 57, 2139–2156. doi:doi:10.1016/S0009-2509(02)00107-0.

Wang, H., You, X., Joshi, A.V., Davis, S.G., Laskin, A., Egolfopoulos, F., Law, C.K., 2007. USC mech version II. High-temperature combustion reaction model of H_2/CO/C_1-C_4 compounds. URL: `http://ignis.usc.edu/USC_Mech_II.htm`. accessed on 12 December 2015.

Wang, Y., Liu, P., Fang, J., Wang, W.N., Biswas, P., 2015. Kinetics of sub-2 nm TiO_2 particle formation in an aerosol reactor during thermal decomposition of titanium tetraisopropoxide. J. Nanoparticle Res. 17, 147. doi:doi:10.1007/s11051-015-2964-y.

West, R.H., Shirley, R., Kraft, M., Goldsmith, C.F., Green, W.H., 2009. A detailed kinetic model for combustion synthesis of titania from $TiCl_4$. Combust. Flame 156, 1764–1770. doi:doi:10.1016/j.combustflame.2009.04.011.

Xiong, Y., Pratsinis, S.E., 1993. Formation of agglomerate particles by coagulation and sintering – Part I. A Two dimensional solution of the population balance equation. J. Aerosol Sci. 24, 283–300. doi:doi:10.1016/0021-8502(93)90003-R.

Yadha, V., Helble, J.J., 2004. Modeling the coalescence of heterogenous amorphous particles. J. Aerosol Sci. 35, 665–681. doi:doi:10.1016/j.jaerosci.2003.11.009.

Yapp, E.K.Y., Chen, D., Akroyd, J., Mosbach, S., Kraft, M., Camacho, J., Wang, H., 2015. Numerical simulation and parametric sensitivity study of particle size distributions in a burner-stabilised stagnation flame. Combust. Flame 162, 2569–2581. doi:doi:10.1016/j.combustflame.2015.03.006.

Yapp, E.K.Y., Patterson, R.I.A., Akroyd, J., Mosbach, S., Adkins, E.M., Miller, J.H., Kraft, M., 2016. Numerical simulation and parametric sensitivity study of optical band gap in a laminar coflow ethylene diffusion flame. Combust. Flame 167, 320 – 334. doi:doi:10.1016/j.combustflame.2016.01.033.

Yu, M., Lin, J., Chan, T., 2008. Numerical simulation of nanoparticle synthesis in diffusion flame reactor. Powder Technol. 181, 9–20. doi:doi:10.1016/j.powtec.2007.03.037.

Zhang, Y., Li, S., Yan, W., Yao, Q., Tse, S.D., 2011. Role of dipole-dipole interaction on enhancing Brownian coagulation of charge-neutral

nanoparticles in the free molecular regime. J. Chem. Phys. 134, 084501. doi:doi:10.1063/1.3555633.

Zhao, B., Uchikawa, K., Wang, H., 2007. A comparative study of nanoparticles in premixed flames by scanning mobility particle sizer, small angle neutron scattering, and transmission electron microscopy. Proc. Combust. Inst. 31, 851–860. doi:doi:10.1016/j.proci.2006.08.064.

Zhao, H., Liu, X., Tse, S.D., 2009. Effects of pressure and precursor loading in the flame synthesis of titania nanoparticles. J. Aerosol Sci. 40, 919–937. doi:doi:10.1016/j.jaerosci.2009.07.004.